Martian dust storm impact on atmospheric water and D/H observed by ExoMars Trace Gas Orbiter

Ann Carine Vandaele[1], Oleg Korablev[2], Frank Daerden[1], Shohei Aoki[1], Ian R. Thomas[1], Francesca Altieri[3], Miguel López-Valverde[4], Geronimo Villanueva[5], Giuliano Liuzzi[5], Michael D. Smith[5], Justin Erwin[1], Loïc Trompet[1], Anna A. Fedorova[2], Franck Montmessin[6], Alexander Trokhimovskiy[2], Denis Belyaev[2], Nikolay Ignatiev[2], Mikhail Luginin[2], Kevin S. Olsen[6], Lucio Baggio[6], Juan Alday[7], Jean-Loup Bertaux[2,6], Daria Betsis[2], David Bolsée[1], Todd Clancy[8], Ed Cloutis[9], Cédric Depiesse[1], Bernd Funke[4], Maia Garcia-Comas[4], Jean-Claude Gérard[10], Marco Giuranna[3], Francisco Gonzalez-Galindo[4], Alexey Grigoriev[2], Yuriy S. Ivanov[11], Jacek Kaminski[12], Ozgur Karatekin[13], Frank Lefèvre[6], Stephen Lewis[14], Manuel López-Puertas[4], Arnaud Mahieux[1], Igor Maslov[2], Jon Mason[14], Michael J. Mumma[5], Lori Neary[1], Eddy Neefs[1], Andrey Patrakeev[2], Dmitry Patsaev[2], Bojan Ristic[1], Séverine Robert[1], Frédéric Schmidt[15], Alexey Shakun[2], Nicholas A. Teanby[16], Sébastien Viscardy[1], Yannick Willame[1], James Whiteway[17], Valérie Wilquet[1], Michael J. Wolff[8], Giancarlo Bellucci[3], Manish R. Patel[14], Jose-Juan Lopez-Moreno[4], François Forget[18], Colin Wilson[7], Håkan Svedhem[19], Jorge L. Vago[19], Daniel Rodionov[2], and the NOMAD and ACS teams

1 Royal Belgian Institute for Space Aeronomy (IASB-BIRA), Brussels, Belgium

2 Space Research Institute (IKI), RAS, Moscow, Russia

3 Istituto di Astrofisica e Planetologia Spaziali (IAPS/INAF), Rome, Italy

4 Instituto de Astrofisica de Andalucia (IAA/CSIC), Granada, Spain

5 NASA Goddard Space Flight Center, Greenbelt, MD, USA

6 LATMOS, UVSQ Université Paris-Saclay, Sorbonne Université CNRS, Paris,France

7 Physics Department, Oxford University, Oxford, UK

8 Space Science Institute, Boulder, Colorado, USA

9 Department of Geography, University of Winnipeg, Winnipeg, Manitoba, Canada

10 LPAP, University of Liège, Liège, Belgium

11 Main Astronomical Observatory MAO NASU, Kyiv, Ukraine

12 Institute of Geophysics, Polish Academy of Sciences, Warsaw, Poland

13 Royal Observatory of Belgium, Brussels, Belgium

14 School of Physical Sciences, The Open University, Milton Keynes, U.K.

15 GEOPS, Univ. Paris-Sud CNRS, Université Paris-Saclay, Orsay, France

16 School of Earth Sciences, University of Bristol, Bristol, UK

17 Centre for Research in Earth and Space Science, York University, Toronto, Ontario, Canada

18 LMD, CNRS Jussieu, Paris, France

19 European Space Agency, Noordwijk, The Netherlands

Global dust storms on Mars are rare events[1,2], but can affect the Martian atmosphere for several months. They can cause changes in atmospheric dynamics and an inflation of the atmosphere[3], primarily due to solar heating of the dust[3]. In turn, changes in atmospheric dynamics can affect the distribution of atmospheric water vapour with potential implications for atmospheric photochemistry and climate on Mars[4]. Recent observations of the Martian atmospheric water vapour abundance during dust storm conditions revealed a high-altitude increase in atmospheric water vapour that was more pronounced at high northern latitudes[5,6], and a decrease in the water column at low latitudes[7,8]. Here we present concurrent, high-resolution measurements of dust, H_2O and HDO at the onset of a global dust storm from the ExoMars Trace Gas orbiter NOMAD and ACS instruments. We report on the vertical distribution of the HDO/H_2O ratio from the planetary boundary layer up to 80 km altitude. Our findings suggest that before the onset of the dust storm, HDO abundances are reduced to below detectability above 40 km altitude. The decrease in HDO

coincides with the observed presence of water-ice clouds. During the storm, an increase in the abundance of H_2O and HDO is observed above 40 km and up to 80 km altitude. We propose that the increased abundances may be the result of warmer temperatures during the dust storm, causing a stronger atmospheric circulation and preventing ice clouds formation, which may confine water vapour to lower altitudes as a result of gravitational fall and subsequent sublimation of ice crystals[3]. The observed changes in H_2O and HDO abundance occurred within a few days during dust storm development, suggesting a fast impact of dust storms on the atmospheric environment.

Although dust is ubiquitous in Mars' atmosphere, global-scale dust storms (GDS) are relatively rare events[1,2] which only occurred twice in the last 17 years (in 2001 and 2007). The physical processes responsible for these phenomena are not yet fully understood, although several mechanisms have been proposed[3]. The ExoMars Trace Gas Orbiter (TGO) arrived at Mars in October 2016 and started its first science observations in April 2018, just before the beginning of the 2018 global dust storm. The NOMAD and ACS instruments on board TGO witnessed the onset and development of this GDS and its impact on water vapour abundance in the Martian atmosphere.

The 2018 GDS started on 30 May near the northern autumn equinox (L_s~185°) and within a few weeks, the planet was covered with atmospheric dust. Instruments on other Mars orbiting and landed spacecraft also witnessed the storm's evolution (e.g. PFS and VMC[9] on board Mars Express, MARCI and MCS[10] on Mars Reconnaissance Orbiter and THEMIS[11] on Mars Odyssey). Observations by Curiosity[12] in Gale Crater indicated that the dust opacity rose from 0.65 on 7 June to 6.7 on 24 June, consistent with the values found by NOMAD and ACS which observed dust opacity to increase by a factor larger than 10 (see Methods).

TGO has a 2-hour orbit and can perform atmospheric measurements during two solar occultation events per orbit when the geometry is favourable. NOMAD and ACS measure the solar radiation spectrum that is filtered by the atmosphere and from which the vertical distribution of atmospheric compounds, in particular, water vapour (both isotopologues, H_2O and HDO), can be retrieved. Atmospheric opacity variation with altitude can also be obtained directly from the decrease in the continuum part of the transmitted solar intensity, thus allowing the instruments to monitor the onset and further evolution of the GDS (Figure 1).

In solar occultation mode, while the TGO-to-Sun line of sight sweeps tangent altitudes above the top of the atmosphere, the sampled line-of-sight optical depth is zero (*i.e.,* no attenuation of the solar signal). When the line of sight to the Sun transects the atmosphere, the line-of-sight optical depth gradually increases, owing to the presence of dust and ice particles, until the atmosphere becomes completely opaque at some tangent altitude. Here the transmittance drops to zero, which usually occurs due to enhanced dust presence in the lowermost part of the atmosphere or, in rarer cases, by the planetary surface. Dust and/or cloud layers in the atmosphere cause local increases in optical depth, with the effect being most pronounced in the equatorial region (Figure 1.D-F). The characteristics of the individual vertical profiles of optical depth vary with latitude, before, during and after the dust storm.

The observations in Figure 1.A-C, made north of 60° latitude, indicate that the continuum line-of-sight optical depth remains low down to 10-20 km tangent altitude throughout the dust storm. The apparent increase with time of the tangent altitude at which the atmosphere becomes opaque is mainly a latitude effect, indicating that the GDS does not impact much the northern latitudes. Some features at 25-40 km altitude were observed from June onwards that were not present before the dust storm: these could be layers of dust that are transported from lower latitudes.

In the mid-latitudes (Figure 1.D-F), before the dust storm, many layers were observed around 40 km. Detached dust layers were previously identified on many occasions[13-15], and their existence has been explained by uplifting during strong convection processes[16-19]. Water ice clouds may be responsible for some of the observed layers, as indicated by observations at other wavelengths and by previous investigations[20-22]. The layers disappear during the dust storm, when the atmosphere is utterly opaque below 40 km because of high dust abundances, and water ice clouds are expected to disappear due to the atmospheric warming in the dust storm[13].

Furthermore, Figure 1.G-I shows the impact of dust/ice clouds in the high southern latitudes, from the beginning of southern spring to the onset of the dusty southern summer season. During the GDS, dust ascended to higher altitudes, comparable to the situation in the mid-latitudes but with more local variability.

On Mars, water vapour has a wide variety of effects on atmospheric photochemistry and climate. Its dissociation by sunlight into hydroxyl radicals controls the overall stability cycle of CO_2. As frost on the surface or as ice clouds in the atmosphere, water exerts a strong influence, leading to large departures from the otherwise dust-controlled radiative balance[3].

Here we present the first water vapour profiles at high vertical resolution (~1 km) that reach down to the planetary boundary layer and extend up to ~80 km (Figure 2 and Figure 3.A). Besides, for the first time, the vertical profile of HDO could be measured (Figure 3.B). The first observations from TGO were carried out prior to the 2018A GDS, and the impact of the global dust storm on the vertical distribution of water vapour and HDO could be monitored. The ACS observations shown in the figures were performed at high southern and northern latitudes, while the NOMAD profiles were obtained in northern mid-latitudes. During the northern autumnal season, when these measurements were carried out, previous column-integrated measurements[7,8] indicated a dry atmosphere at high latitudes caused by the developing seasonal polar cap in the North and its receding counterpart in the South. Temperatures are cold enough to condense out CO_2 and as a consequence also water vapour will be removed from the lower atmosphere by condensation into clouds and subsequent sedimentation[3]. The seasonal cap development therefore explains the very low water abundances in the lowest 20 km for the sub-polar profiles (Figure 2). The profiles observed before the dust storm indicate low abundances of water vapour above 60 km, with values below 10 ppm, and with large error bars. Profiles from the southern hemisphere are shown in Figure 2.B and Figure 3.A; they correspond to the southern summer season with a lot of dust present in the atmosphere already before the GDS, explaining the cut-off at ~15 km. Northern hemisphere profiles were taken in more dust free conditions and reach down to ~4 km.

Water profiles, both H_2O and HDO, show a large enhancement in the middle atmosphere after the onset of the dust storm. The increase in water abundance is observed above 20 km, with water vapour being lifted upwards up to at least 80 km. Previous studies have reported a sharp decrease of the total water column in the equatorial region[7,8], indicative of redistribution of water vapour in a dust storm. Previous measurements[5] of water vapour profiles already exhibited an increase of the atmospheric water content at high altitudes and latitudes, as is confirmed by these new data. This phenomenon was also linked to an increase in the escape of hydrogen from Mars' atmosphere[6,23]. What is remarkable in the observations presented here (Figure 2), is that this enhancement is happening very fast, in the course of just a few days during the onset of the dust storm (around 7-8 June, Ls~188-190°).

The observed changes in the distribution of atmospheric water reported here can be understood as resulting from a variety of processes. The higher abundance of dust heats large parts of the atmosphere because of the absorption of solar radiation by the dust particles. Dust absorption and the subsequent warming of the surrounding gas causes an expansion of the atmosphere, which leads to a redistribution of water vapour to a wider vertical range. The higher atmospheric temperatures at low and middle latitudes and the resulting higher thermal contrast between the equatorial and polar regions also strengthen the mean meridional circulation, this leads to an additional redistribution of water vapour across latitude. Also because of the higher temperatures, fewer water ice clouds are expected to be present during a dust storm. Under non-dust storm conditions, the formation of clouds acts to confine water vapour to lower altitudes due to the gravitational fall and subsequent sublimation of ice crystals. In addition, numerical modelling has also demonstrated that solar heating of atmospheric dust can drive localized deep convection[17,18] and larger scale ascent of dust layers[19] that would, along with the dust, also transport water vapour to higher altitudes. All these processes that contribute to explaining the observed changes in the water vapour profiles have been quantitatively demonstrated with global circulation models and by data assimilation of water vapour in previous years on Mars[3,24-26]. For a more quantitative understanding of the 2018 GDS, more detailed modelling and assimilation studies that simulate the transition from normal to global dust storm conditions[3,24,25,27] will have to be performed, using dust constraints derived from instruments that monitored the GDS, including TGO instruments.

The fractionation between H_2O and HDO is an important process in planetary atmospheres. The D/H ratio is a marker of the evolution of the water inventory on Mars[28]. On Mars, the D/H budget is dominated by H_2O and HDO which are the unique precursors of the escaping D and H atoms above the exobase. HDO was previously measured as column-integrated abundances from Earth[29-31] and *in situ*[32] by the Mars Science Laboratory. NOMAD and ACS provide for the first time the capability to observe the vertical distribution of HDO simultaneously with water vapour, thereby providing key information on the fractionation processes that are expected to control the amount of hydrogen and deuterium atoms escaping to space[3]. H_2O and HDO are fractionated during photolysis and ice formation[33]. NOMAD observations (Figure 3) reveal that the HDO density profiles during the pre-storm period exhibit a sudden decline at 40-45 km altitude, just below a layer of water ice clouds, consistent with this view (see Methods). ACS observations show this decrease to occur at 50 km but were taken at a different latitude, where the hygropause may be located at a different altitude. The HDO/H_2O ratio is similar in both profiles below 45 km: 4-6 VSMOW (Vienna Standard Mean Ocean Water). HDO is distinctly more abundant at high altitudes during the dust storm than before the storm. We suggest that this might be the result of the strong atmospheric warming during the GDS, which causes the hygropause to ascend to higher altitudes. The HDO/H_2O ratio is relatively similar before and during the GDS, which demonstrates that HDO is advected along with H_2O to higher altitudes and latitudes during the onset of the GDS.

Fractionation of HDO and H_2O is expected to occur during condensation of both isotopologues[33]. Model studies predict that by condensation and cloud sedimentation, the abundances of H_2O and HDO become very small above the hygropause[4,33]. This is confirmed by our first results (Figure 3). The coincidence of a strong decrease in HDO, below detectability, with an observed water ice cloud, may provide the first direct indication of the fractionation process. Because of the fractionation effect, HDO is expected to be relatively more concentrated into the ice cloud and thus more scavenged from the condensation level, such that the HDO/H_2O ratio is expected to decrease with altitude. The effect of the dust storm is to expand the atmosphere and to lift up the hygropause. Continued measurements by TGO shall permit us to unveil both the spatial and the seasonal trends of D/H.

References

1 Shirley, J. H., Newman, C., Mischna, M. & Richardson, M. Replication of the historic record of martian global dust storm occurrence in an atmospheric general circulation model. *Icarus* **317**, 197-208, doi:https://doi.org/10.1016/j.icarus.2018.07.024 (2019).

2 Montabone, L. *et al.* Eight-year climatology of dust optical depth on Mars. *Icarus* **251**, 65-95 (2015).

3 Haberle, R. M., Clancy, R. T., Forget, F., Smith, M. D. & Zurek, R. W. *The atmosphere and climate of Mars*. (Cambridge University Press, 2017).

4 Daerden, F. *et al.* Mars atmospheric chemistry simulations with the GEM-Mars general circulation model. *Icarus* **online 1 March 2019**, doi:https://doi.org/10.1016/j.icarus.2019.02.030 (2019).

5 Fedorova, A. *et al.* Water vapor in the middle atmosphere of Mars during the 2007 global dust storm. *Icarus* **300**, 440-457 (2018).

6 Heavens, N. G. *et al.* Hydrogen escape from Mars enhanced by deep by deep convection in dust storms. *Nature Letters* **2**, 126-132, doi:10.1038/s41550-017-0353-4 (2018).

7 Smith, M., Daerden, F., Neary, L. & Khayat, A. The climatology of carbon monoxide and interannual variation of water vapor on Mars as observed by CRISM and modeled by the GEM-Mars general circulation model. *Icarus* **301**, 117-131, doi:https://doi.org/10.1016/j.icarus.2017.09.027 (2018).

8 Trokhimovsky, A. *et al.* Mars' water vapor mapping by the SPICAM IR spectrometer: Five martian years of observations. *Icarus* **251**, 50-64 (2015).

9 Sanchez-Lavega, A. *et al.* in *AGU Fall Meeting 2018.*

10 Schoffield, J. T., Kleinbohl, A., Kass, D. & McCleese, D. in *42nd COSPAR Scientific Meeting* (Pasadena, CA, USA, 14-22 July, 2018).

11 Smith, M. D. in *AGU Fall Meeting 2018.*

12 Vasada, A., Crisp, J. & Meyer, M. in *42nd COSPAR Scientific Meeting* (Pasadena, CA, USA, 14-22 July, 2018).

13 Guzewich, S., Talaat, E., Toigo, A., Waugh, D. W. & McConnochie, T. High-altitude dust layers on Mars: Observations with the Thermal Emission Spectrometer. *J. Geophys. Res. Planets* **118**, 1177–1194, doi:doi:10.1002/jgre.20076 (2013).

14 Heavens, N. G. *et al.* Seasonal and diurnal variability of detached dust layers in the tropical Martian atmosphere. *J. Geophys . Res .: Planets* **119**, 1748-1774, doi:10.1002/2014JE004619 (2014).

15 Määttänen, A. *et al.* A complete climatology of the aerosol vertical distribution on Mars from MEx/SPICAM UV solar occultations. *Icarus* **223**, 892-941, doi:http://dx.doi.org/10.1016/j.icarus.2012.12.001 (2013).

16 Wang, C. *et al.* Parameterization of Rocket Dust Storms on Mars in the LMD Martian GCM: Modeling Details and Validation. *J. Geophys . Res .* **123**, 982-1000, doi:https://doi.org/10.1002/2017JE005255 (2018).

17 Rafkin, S. The potential importance of non-local, deep transport on the energetics, momentum, chemistry,and aerosol distributions in the atmospheres of Earth, Mars, and Titan. *Planetary and Space Science* **60**, 147-154, doi:10.1016/j.pss.2011.07.015 (2012).

18 Spiga, A., Faure, J., Madeleine, J. B., Maattanen, A. & Forget, F. Rocket dust storms and detached dust layers in the Martian atmosphere. *J. Geophys . Res .* **118**, 746-767, doi:10.1002/jgre.20046 (2013).

19 Daerden, F. *et al.* A Solar Escalator on Mars: Self-Lifting of Dust Layers by Radiative Heating. *Geophys. Res. Lett.* **42**, 7319–7326, doi:doi:10.1002/2015GL064892 (2015).

20 Clancy, R. T. *et al.* Extension of atmospheric dust loading to high altitudes during the 2001 Mars dust storm: MGS TES limb observations. *Icarus* **207**, 98-109 (2010).

21 Sefton-Nash, E. *et al.* Climatology and first-order composition estimates of mesospheric clouds from Mars Climate Sounder limb spectra. *Icarus* **222**, 342-356, doi:https://doi.org/10.1016/j.icarus.2012.11.012.

22 McCleese, D. J. *et al.* Structure and dynamics of the Martian lower and middle atmosphere as observed by the Mars Climate Sounder: Seasonal variations in zonal mean temperature, dust, and water ice aerosols. *J. Geophys. Res.* **115**, E12016, doi:doi:10.1029/2010JE003677 (2010).

23 Chaffin, M. S., Deighan, J., Schneider, N. M. & Stewart, A. I. F. Elevated atmospheric escape of atomic hydrogen from Mars induced by high-altitude water. *Nature Geoscience* **10**, 174-178, doi:DOI: 10.1038/NGEO2887 (2017).

24 Forget, F. *et al.* Improved general circulation models of the Martian atmosphere from the surface to above 80 km. *J. Geophys . Res .* **104**, 24155-24175 (1999).

25 Neary, L. & Daerden, F. The GEM-Mars General Circulation Model for Mars: Description and Evaluation. *Icarus* **300**, 458–476, doi:https://doi.org/10.1016/j.icarus.2017.09.028 (2018).

26 Steele, L. *et al.* The seasonal cycle of water vapour on Mars from assimilation of Thermal Emission Spectrometer data. *Icarus* **237**, 97-115, doi:http://dx.doi.org/10.1016/j.icarus.2014.04.017 (2014).

27 Lewis, S. R. *et al.* The solsticial pause on Mars: 1. A planetary wave reanalysis. *Icarus* **264**, 456-464, doi:https://doi.org/10.1016/j.icarus.2015.08.039 (2016).

28 Lammer, H. *et al.* Outgassing History and Escape of the Martian Atmosphere and Water Inventory. *Space Sci. Rev.* **174**, 113-154 (2013).

29 Encrenaz, T. *et al.* New measurements of D/H on Mars using EXES aboard SOFIA. *Astron. Astrophys.* **612**, A112 (2018).

30 Aoki, S. *et al.* Seasonal variation of the HDO/H_2O ratio in the atmosphere of Mars at the middle of northern spring and beginning of northern summer. *Icarus* **260**, 7-22, doi:http://dx.doi.org/10.1016/j.icarus.2015.06.021 (2015).

31 Villanueva, G. *et al.* Strong water isotopic anomalies in the martian atmosphere: Probing current and ancient reservoirs. *Science* **348**, 218-221 (2015).

32 Webster, C. R. *et al.* Isotope Ratios of H, C and O in CO_2 and H_2O of the Martian Atmosphere. *Science* **341**, 260-263, doi:10.1126/science.1237961 (2013).

33 Montmessin, F., Fouchet, T. & Forget, F. Modeling the annual cycle of HDO in the Martian atmosphere. *J. Geophys. Res.* **110**, doi:10.1029/2004JE002357 (2005).

Competing interest

The authors declare no competing financial interests.

Acknowledgments

ExoMars is a space mission of ESA and Roscosmos. The NOMAD experiment is led by the Royal Belgian Institute for Space Aeronomy (IASB-BIRA), assisted by Co-PI teams from Spain (IAA-CSIC), Italy (INAF-IAPS), and the United Kingdom (Open University). This project acknowledges funding by the Belgian Science Policy Office (BELSPO), with the financial and contractual coordination by the ESA Prodex Office (PEA 4000103401, 4000121493), by Spanish MICINN through its Plan Nacional and by European funds under grants ESP2015-65064-C2-1-P and ESP2017-87143-R (MINECO/FEDER), as well as by UK Space Agency through grants ST/R005761/1, ST/P001262/1, ST/R001405/1, ST/S00145X/1, ST/R001367/1, ST/P001572/1 and ST/R001502/1 and Italian Space Agency through grant 2018-2-HH.0. The IAA/CSIC team acknowledges financial support from the State Agency for Research of the Spanish MCIU through the "Center of Excellence Severo Ochoa" award for the Instituto de Astrofísica de Andalucía (SEV-2017-0709). This work was supported by the Belgian Fonds de la Recherche Scientifique - FNRS under Grant n°30442502 (ET_HOME). The ACS experiment is led by IKI, Space Research Institute in Moscow, assisted by LATMOS in France. The project acknowledges funding by Roscosmos and CNES. Science operations of ACS are funded by Roscosmos and ESA. IKI affiliates acknowledge funding under grant #14.W03.31.0017 and contract #0120.0 602993 (0028-2014-0004) of Russian Government.

We are grateful to all ESA ESOC, ESAC, and IKI Science Operations Center personnel, whose efforts made the success of TGO possible.

Author contributions

ACV and OK conceived the study, collected inputs and wrote the paper. SA, GV, GL retrieved trace gas abundances, in particular those of H_2O and HDO from the NOMAD instrument. IRT analysed the

SO solar occultation data. LT provided transmittances from the NOMAD SO v0.3a. JTE and SR provided and analysed the a priori knowledge and initial GCM fields. FD and LN provided the GCM fields. SV, FGG, FL, SL, and JK provided the global circulation model background and discussion. FA, OzK and VW are coordinating the dust observations between IR and UVIS, and nadir and occultation. MLV, JCG, MGC, MLP, BF analysed the NOMAD limb data. MLP provided the dust profiles from NOMAD IR data. MS, TC, and MW provided contextual information from Themis/MO instrument. MG provided contextual information from PFS/MEX. M.M. provided support for the spectroscopic parameters selection. FS, NAT provided alternative methods to derive detection of trace gases from IR NOMAD. JW, EC provided support for the selection of the surface properties. AM gave support to the calibration of the IR channels. CD, DB and YW were involved in UVIS calibration and data pipeline. BR and EN designed the NOMAD observations helped by JM for the UVIS channel. AAF calibrated the ACS NIR data and analysed the water profiles assisted with FM, AT, DBet, and JLB. CO_2 data was analysed by DBel The ACS datasets were prepared for NIR by AT and AP and for TIRVIM by NI, AS, IM, AT, and AG have designed the ACS observations. ML and DP have analysed the TIRVIM occultation profiles. KO, JAP, and LB provided support for the water retrieval. YI helped in the MIR calibration. MRP, GB and JJLM provided support in the selection of the NOMAD observations based on scientific interest. FF, CW, DR, JLV and HS Coordinated the observations of the various instruments on the TGO. All authors assisted ACV and OK with the preparation of the manuscript.

Correspondence

Correspondence and requests for materials should be addressed to a-c.vandaele@aeronomie.be

Additional information

Reprints and permissions information available at www.nature.com/reprints

Figure captions

Figure 1: Evolution of the dust/cloud extinction obtained by the NOMAD SO channel during the onset of the global dust storm: from the first observations in April and May (left panels) to the August-September 2018 timeframe (right panels), spanning Ls = 163° to 246° (late northern summer to autumn). The data , consisting of 536 individual measurements, is split into 3 latitude bins, with the colour of the line indicating the latitude within each bin. The latitudinal coverage is dependent on the orbit and solar position, and so the latitude ranges were selected based on the data available: northern profiles for latitude > 60°N (upper panels); mid-latitude profiles for latitudes between -30°S and 30°N (middle panels); and southern profiles for latitudes between -70°S and -50°S (lower panels). In the early phase of the TGO mission, more solar occultations occurred near the northern pole, as is evident in the figures. Plotted here is the continuum line-of-sight optical depth versus tangent altitude of the centre of the line of sight above the Mars reference areoid. The line-of-sight optical depth is inferred from the transmittance after the removal of atmospheric absorption lines. Diffraction order 121 was used for this study, covering the 2720-2740 cm^{-1} spectral range. Horizontal error bars are not shown here, as they are very small: for an SNR of 1000, the 1-sigma error is 0.003 units for an optical depth of 1, and 0.06 units for an optical depth of 4.

Figure 2: H_2O volume mixing ratio (vmr) profiles observed by ACS NIR, during the onset of the global dust storm . Left: northern latitudes; black: Ls = 188.28° – Lat = 77.5° N; blue: Ls = 188.75° – Lat = 76.4° N; green: Ls = 189.41° – Lat = 74.8° N; yellow: Ls = 189.90° – Lat = 73.8° N. Right: southern latitudes; blue: Ls = 188.62° – Lat = 68.2° S; cyan: Ls = 189.19° – Lat = 70.0° S; yellow: Ls = 189.67° – Lat = 71.3° S; orange: Ls = 190.05° – Lat = 72.4° S; red: Ls = 190.50° – Lat = 73.8° S. Water abundances were deduced from ACS NIR observations (order 56 covering the 1.38 μm band, 7225-7300 cm^{-1}; the CO_2 density was measured in order 49, 6320-6390 cm^{-1}). The uncertainty in the local number densities is given by the covariance matrix of the solution error (as described in the text).

Figure 3: H_2O, HDO and D/H detections before and during the storm. Panel A: NOMAD H_2O observations before the storm (blue: Ls: 171.45°, Lat: 43°N to 68°N), and during the storm (red: Ls: 196.64°, Lat: 51°N to 59°N,) and ACS MIR observations before the storm (cyan: Ls: 168.75°, Lat: 39°S to 43°S), and during the storm (yellow: Ls: 196.64°, Lat: 80°S to 83°S). The corresponding HDO VMR profiles are shown in Panel B. Panel C shows the D/H ratio obtained for each of the H_2O-HDO observations. All errors in Panel A–C are 1σ. VSMOW is the Vienna Standard Mean Ocean Water reference value, 312 ppm HDO/H_2O.

Methods

The NOMAD instrument and dataset. NOMAD, the "Nadir and Occultation for MArs Discovery" spectrometer suite[34-36], is part of the payload of the ExoMars 2016 Trace Gas Orbiter mission[37]. The instrument is conducting a spectroscopic survey of Mars' atmosphere in ultraviolet (UV), visible and infrared (IR) wavelengths covering large parts of the 0.2-4.3 µm spectral range. NOMAD is composed of three spectrometers: a solar occultation only spectrometer (SO – Solar Occultation) operating in the infrared (2.3-4.3 µm), a second infrared spectrometer (2.3-3.8 µm) capable of nadir, but also solar occultation and limb observations (LNO – Limb Nadir and solar Occultation), and an ultraviolet/visible spectrometer (UVIS – UV visible, 200-650 nm) that also has all three observation modes. The spectral resolution of SO (0.15 cm^{-1} at 3000 cm^{-1}) surpasses previous surveys from orbit in the infrared by at least one order of magnitude. NOMAD offers an integrated instrument combining a flight-proven concept and innovations based on existing instrumentation: SO is a copy of the Solar Occultation in the IR (SOIR) instrument[38] on Venus Express (VEx[39]), LNO is a modified version of SOIR, and UVIS has heritage from the development in the context of the Humboldt lander. NOMAD provides vertical profiling for atmospheric constituents at unprecedented spatial and temporal resolution. Indeed, in solar occultation, the vertical resolution is less than 1 km for SO and UVIS, with a sampling rate of 1 s (one measurement every 1 km), and occultations range from the surface to 200 km altitude. NOMAD also provides mapping of several constituents in nadir mode with an instantaneous footprint of 0.5 x 17 km^2 (LNO spectrometer) and 5 km^2 (UVIS spectrometer), with a repetition rate of 30 Martian days.

For this work we analysed SO channel data measured between 21 April and 30 September. SO measures 4 spectra for 5 or 6 different diffraction orders per second in solar occultation mode.

The ACS instrument and dataset. ACS[40] consists of three infrared channels featuring high accuracy, high resolving power, and a broad spectral coverage (0.7 to 17 µm). The near-infrared (NIR) channel is based on the principle of echelle-spectrometer with selection of diffraction orders by an acousto-optical tuneable filter (AOTF). The same principle was employed by SOIR on VEx[4] and by the infrared channels of NOMAD described above. ACS NIR covers a spectral range of 0.7-1.7 μm in diffraction orders 101 through 49. The instrument capitalises at the science heritage of SPICAM-IR[41] on board ESA's Mars Express, benefiting from much higher resolving power of $\lambda/\Delta\lambda\approx25{,}000$. During an occultation ACS NIR measures 10 preselected diffraction orders in two seconds, including the absorption bands of H_2O at 1.13, 1.38, and 1.40 μm, and CO_2 at 1.27, 1.43, 1.54, and 1.57 μm. The mid-infrared (MIR) channel is a newly developed crossed dispersion echelle spectrometer dedicated to solar occultation measurements in the 2.3-4.5 μm range. The spectral resolving power is $\lambda/\Delta\lambda\approx50{,}000$. For each acquired frame MIR measures up to 20 adjacent diffraction orders, covering an instantaneous spectral range of 0.15-0.3 μm. To achieve the full spectral coverage a secondary dispersion grating can be rotated to one out of 11 positions. The H_2O and HDO profiles can be measured simultaneously by MIR using the positions 4, 5 and 11.

The concept of Fourier-transform spectrometer TIRVIM is close to that of Planetary Fourier Spectrometer (PFS[42]) on board MEx, though TIRVIM features a cryogenic detector and the solar occultation capability. In occultation, TIRVIM is operated mostly in 'climatology' mode, covering instantaneously, each 0.4 s, the full spectral range of 1.7-17 μm (effectively 1.7-5 μm) with spectral resolution ≤ 1 cm^{-1}. These three channels are used to observe in solar occultation; NIR and TIRVIM are operated also in nadir to measure atmospheric gases and to characterise the atmospheric state: dust loading and condensation clouds. The atmospheric temperature profile is retrieved from the 15-μm CO_2 band measured by TIRVIM in nadir.

In this work we used NIR occultation profiles (Figure 2) obtained at high latitudes in the southern and northern hemispheres (see ED Table 1). MIR simultaneous H_2O and HDO profiles (Figure 3) were obtained in the southern hemisphere in order 224 (position 4 of secondary grating). TIRVIM aerosol profiling (ED Figure 7) was done using solar occultation data obtained in the southern hemisphere, orbit 2556, Ls=197°, latitude 81°S during the egress (local time 9:26), i.e. during the same occultation of the MIR results shown in Figure 3.

Solar occultation technique. The solar occultation technique is a powerful method to gain information on the vertical structure of atmospheres. At sunset, the recording of spectra starts well before the occultation occurs (the solar spectrum outside the atmosphere is used for referencing), and continues until the line of sight crosses the planet. At sunrise, the recording of spectra continues well above the atmosphere to provide the corresponding reference. Transmittances are obtained by dividing the spectra measured through the atmosphere by the reference spectrum recorded outside the atmosphere[43]. In this way, transmittances become independent of instrumental characteristics, such as the absolute response or the ageing of the instrument and in particular of the detector. Such observations provide high vertical resolution (< 1 km for NOMAD SO and ACS NIR and 2.0-2.5 km for ACS MIR observations) profiles of the structure and composition of the atmosphere. ACS TIRVIM observes the full Sun disk during an occultation, resulting in a coarser vertical resolution (~9 km).

Profiles of dust extinction. To calculate the extinction due to dust and/or clouds, it is necessary to remove the absorption lines of atmospheric gas species, leaving the background continuum. For the analysis here, diffraction order 121 of NOMAD SO was chosen, as 1) this order is measured routinely, so has high spatial/temporal coverage and 2) it is relatively simple to remove the atmospheric absorption lines. A 4th order polynomial is fitted to the data. The optical depths in Figure 1 are inferred from the value of the continuum in the centre of the detector (pixel 160). The fitting algorithm fails at low and high altitudes, where either the absorption lines from molecular species are saturated or the signal is so low that it is effectively noise. Therefore, any spectra where transmittance > 99.5% are assumed to have an optical depth of 0, and points where transmittance < 0.5% are not plotted; hence the lines end abruptly at low altitudes when the optical depth becomes high. The observations in Figure 1 are split into North, South and mid-latitudes using the following criteria: greater than 60° North, between -70° and -50° South, and between -30° and +30° for the mid-latitudes. The tangent altitude is calculated as the shortest distance between the line of sight of the centre of the field of view and the MGM1025 Areoid (i.e. the Mars geoid)[44]. The latitude is the point on the areoid closest to the centre of the field of view, i.e. the tangent point, at the midpoint of the solar occultation measurement. The characteristics of the individual vertical profiles of optical depth vary with latitude, as seen when optical depth is plotted vs latitude and Mars longitude (ED Figure 1).

To further investigate the impact of the dust storm, two orbits covering the same footprint and solar illumination conditions on Mars have been considered; they were acquired by the nadir channel of NOMAD, respectively, before (April 26th) and during (July 11th) the global dust storm. ED Figure 2 compares the dust radiance signature before and after the storm, but in contrast to Figure 1, now in a nadir geometry and in a different wavelength, at 2.3 μm. Comparison with radiative transfer modelling suggests a factor of ~10 increase in opacity at 2.3 μm during the storm. Note also how the surface albedo features are obscured by the increase of the atmospheric dust load. The radiance variation with latitude is mainly dominated by the total albedo (surface + atmosphere) and solar zenith angle, which varies along the track. The radiative transfer model includes multiple scattering and a layered atmosphere with pressure/temperature profiles from the LMD General Circulation Model[45]. Further details on the radiative transfer model can be found in Villanueva, et al. [46].

Vertical profiles of H_2O and HDO volume mixing ratio. The vertical profiles of H_2O and HDO volume mixing ratio are investigated from the NOMAD dataset shown in ED Table 1. These NOMAD spectra are all taken in the northern hemisphere at the same local time (at 18h). The NOMAD SO channel can record spectra for multiple diffraction orders during an occultation. The occultation performed on 7 May includes the measurements of diffraction order 168 (3775.53 – 3805.63 cm^{-1}) and order

136 (3056.39 – 3080.75 cm^{-1}) where strong H_2O lines are present and of order 119 (2674.34 – 2695.65 cm^{-1}) with strong HDO lines. The occultation measurement on 20 June contains two diffraction orders for H_2O - order 168 and 134 (3011.44 – 3035.44 cm^{-1}), and diffraction order 121 for HDO (2719.28 – 2740.96 cm^{-1}) (ED Figure 3).

We retrieved H_2O volume mixing ratio using the whole spectral range of those diffraction orders, in order to maximize the information content at every occultation tangent altitude. In this study, CO_2 and H_2O gas absorptions were included. The absorption coefficients of these gases are calculated based on a line-by-line method using the water vapour line list for a CO_2-rich atmosphere for H_2O[47,48] and HITRAN 2016[49] for CO_2. Temperature, pressure, and CO_2 volume mixing ratio are taken from the values predicted by GCMs for each altitude. The calculated synthetic spectra are convolved with a Gaussian function that corresponds to the spectral resolving power of the NOMAD SO channel (R=11000-15000). The final synthetic spectra are then built by considering an instrument model that comprises the effects of the Acousto-Optic Tunable Filter (AOTF) and the grating (i.e., Blaze function)[50]. The free parameters in the retrievals are the vertical profiles of volume mixing ratio and the parameters for the polynomial function to model the continuum of each spectrum. Retrievals are performed using an Optimal Estimation approach[51] implemented in a Gauss-Newton iterative scheme. ED Figure 4 shows an example of fit results.

The water vapour profiles shown in Figure 2 are retrieved from the ACS NIR spectra (see also ED Table 1). Wavelength drift is corrected using positions of gaseous absorption lines. The spectra fitting and the profile retrieval follow the method described for SPICAM MEx 1.38-µm band[5,52]. All the altitudes of the profiles are fitted simultaneously (global fit) using a Levenberg–Marquardt iterative algorithm[53,54]. Tickhonov regularization is then applied, customary for vertical inversions in order to smooth the profile. The uncertainty in the local number densities is given by the covariance matrix of the solution errors. The water vapour abundances were retrieved from spectra acquired in diffraction order 56 (covering the 1.38 µm band, or 7220-7300 cm^{-1}). ED Figure 5 shows an example of fit results. The spectral line parameters for H_2O are taken from HITRAN 2016[49] with a correction coefficient for the CO_2 rich atmosphere[5]. Temperature and pressure for the radiative transfer computations are taken from the MCD[45] global circulation model (GCM). To obtain the VMR profiles of water vapour, the CO_2 density was retrieved from ACS NIR spectra in order 49, 6320-6390 cm^{-1}.

The vertical profiles of H_2O and HDO volume mixing ratio investigated from the ACS dataset (Figure 3.B and C) were obtained in the southern hemisphere at middle and high latitudes (ED Table 1). During these observations MIR channels recorded spectra at position 4 (diffraction orders 210-224). To obtain the H_2O and HDO density the order 224 (3763-3775 cm^{-1}) was used for both observations in 2th May and 20th June. We retrieved H_2O and HDO volume mixing ratio using several lines present in this diffraction order. The spectral line parameters for H_2O are taken from HITRAN 2016 with a correction coefficient for the CO_2 braodening[5]. Temperature and pressure for radiative transfer computations are taken from GCM MCD[45]. The calculated synthetic spectra are convolved with a Gaussian function that corresponds to the spectral resolving power of the ACS MIR channel (R~30000-35000).

For both NOMAD and ACS, the D/H values are obtained by dividing the HDO and H_2O densities retrieved at the same altitude. The D/H errors are calculated by weighted average: D/H_Error = [D/H] * sqrt((HDO_error/[HDO])$^{\wedge 2}$ + (H2O_error/[H2O])$^{\wedge 2}$), where [] are used to indicate the density. Because the H_2O and HDO are retrieved independently and coming from different datasets (here different orders and different absorption lines), they are truly independent. The error-bars are therefore non-correlated. The error-bars capture the instrumental systematic effects, since they are based on the final chi-square

Water ice clouds. ED Figure 6 shows the aerosol optical depth derived from NOMAD SO on May 7th, 2018 before the dust storm, during which orders 119, 136, 148, 168 and 189 were measured, corresponding to the central wavenumbers 2685.0, 3068.0, 3339.0, 3790.0, and 4265.0 cm^{-1} respectively. The optical depths have been derived by averaging the transmittances with a sampling of 3 km, and deriving for each tangent height the equivalent optical depth rescaled by the occultation path. Each optical depth has been determined simultaneously with the abundances of the other gases detectable in each order; hence a full retrieval is used. Each spectrum has been processed with the Planetary Spectrum Generator (PSG[46]) forward model and a retrieval scheme based on Optimal Estimation in a Gauss-Newton iterative scheme. Optical depth is derived for each single sampled altitude, and is compared to the extinction of water ice with different particle sizes (Top panel of ED Figure 6). This Figure shows that the detached layer observed by NOMAD at 40-50 km is a water ice cloud with particle sizes between 0.1 and 1 μm.

Aerosol properties from TIRVIM solar occultation data were retrieved from 20 wavenumbers in the spectral range of 1500−4500 cm^{-1} chosen outside of strong gas absorption bands. This channel is operated continuously, and therefore remains very stable during an occultation. To increase signal-to-noise ratio, spectra are averaged using simple moving mean within 50 cm^{-1} spectral window centred at the chosen wavenumbers, spectra errors were calculated as s.e.m with $n = 78$. The procedure to obtain transmittances from the TIRVIM dataset is straightforward. This channel is operated continuously, and therefore remains very stable during an occultation. Slant optical depth is calculated as $\tau_v(L) = -\ln(T(L))$, where T is the transmittance over the line of sight L. Transmission and slant optical depth errors are calculated using propagation of uncertainty formulas. Vertical profiles of extinction and corresponding errors are retrieved using the standard 'onion peeling' method in Fedorova, et al. [55]. Further steps involve Mie modelling of the spectral dependence of the extinction coefficient assuming known optical properties for the aerosols[56,57] fit to the experimental data to retrieve vertical profiles of the size distribution and number density as described in

Fedorova, et al. [58]. A log-normal size distribution[59] of the aerosol particles with a width (the effective variance) of 0.3 was assumed. To distinguish between water ice and dust particles, we apply the optimal estimation retrieval scheme independently for both types, and make the decision based on the fit quality (ED Figure 7). The algorithm is able to retrieve the number density (typically ~1 particles cm^{-3}), and the effective radius (1–1.5 µm). Errors on these values are estimated from the covariance matrix.

References

5 Fedorova, A. *et al.* Water vapor in the middle atmosphere of Mars during the 2007 global dust storm. *Icarus* **300**, 440-457 (2018).

34 Vandaele, A. C. *et al.* NOMAD, an integrated suite of three spectrometers for the ExoMars Trace Gas mission: technical description, science objectives and expected performance. *Space Sci. Rev.* **214:80**, doi.org/10.1007/s11214-11018-10517-11212, doi:https://doi.org/10.1007/s11214-018-0517-2 (2018).

35 Neefs, E. *et al.* NOMAD spectrometer on the ExoMars trace gas orbiter mission: part 1—design, manufacturing and testing of the infrared channels. *Applied Optics* **54**, 8494-8520, doi:http://dx.doi.org/10.1364/AO.54.008494 (2015).

36 Patel, M. R. *et al.* The NOMAD spectrometer on the ExoMars Trace Gas Orbiter mission: part 2—design, manufacturing and testing of the ultraviolet and visible channel. *Applied Optics* **56**, 2771-2782, doi:https://doi.org/10.1364/AO.56.002771 (2017).

37 Svedhem, H. *et al.* The ExoMars Trace Gas Orbiter. *Space Sci. Rev.* **214**, (in press) (2018).

38 Nevejans, D. *et al.* Compact high-resolution space-borne echelle grating spectrometer with AOTF based on order sorting for the infrared domain from 2.2 to 4.3 micrometer. *Applied Optics* **45**, 5191-5206 (2006).

39 Titov, D. V. *et al.* Venus Express: Scientific Goals, Instrumentation and Scenario of the Mission. *Cosmic Res.* **44**, 334-348 (2006).

40 Korablev, O. *et al.* The Atmospheric Chemistry Suite (ACS) of three spectrometers for the ExoMars 2016 Trace Gas Orbiter. *Space Sci. Rev.* **214: 7**, https://doi.org/10.1007/s11214-11017-10437-11216 (2018).

41 Korablev, O. *et al.* SPICAM IR acousto-optic spectrometer experiment on Mars Express. *J. Geophys. Res.* **111**, 1-17 (2006).

42 Formisano, V. *et al.* The Planetary Fourier Spectrometer (PFS) onboard the European Mars Express mission. *Planet. Space Sci.* **53**, 963-974 (2005).

43 Trompet, L. *et al.* Improved algorithm for the transmittance estimation of spectra obtained with SOIR/Venus Express. *Applied Optics* **55**, 9275-9281, doi:http://dx.doi.org/10.1364/AO.55.009275 (2016).

44 Lemoine, F. G. *et al.* An improved solution of the gravity field of Mars (GMM-2B) from Mars Global Surveyor. *J. Geophys. Res.* **106**, 23,359–323,376 (2001).

45 Millour, E. *et al.* (2015).

46 Villanueva, G., Smith, M., Protopasa, S., Faggi, S. & Mandell, A. M. Planetary Spectrum Generator: an accurate online radiative transfer suite for atmospheres, comets, small bodies and exoplanets. *J. Quant. Spectrosc. Radiat. Transfer* **217**, 86-104 (2018).

47 Devi, V. M. *et al.* Line parameters for CO_2- and self-broadening in the nu3 band of $HD^{16}O$. *J. Quant. Spectrosc. Radiat. Transfer* **203**, 158-174 (2017).

48 Devi, V. M. *et al.* Line parameters for CO_2- and self-broadening in the nu1 band of $HD^{16}O$. *J. Quant. Spectrosc. Radiat. Transfer* **203**, 133-157 (2017).

49 Gordon, I. E. *et al.* The HITRAN2016 Molecular Spectroscopic Database. *J. Quant. Spectrosc. Radiat. Transfer* **203**, 3-69, doi:doi:10.1016/j.jqsrt.2017.06.038 (2017).

50 Liuzzi, G. *et al.* Methane on Mars: new insights into the sensitivity of CH4 with the NOMAD/ExoMars spectrometer through its first in-flight calibration. *Icarus* **321**, 671-690, doi:doi:10.1016/j.icarus.2018.09.021 (2018).

51 Rodgers, C. D. *Inverse methods for atmospheric sounding: Theory and practice*. (University of Oxford, 2000).

52 Maltagliati, L. *et al.* Annual survey of water vapor vertical distribution and water–aerosol coupling in the martian atmosphere observed by SPICAM/MEx solar occultations. *Icarus* **223**, 942-962 (2013).

53 Levenberg, K. A method for the solution of certain non-linear problems in least squares. *Quarterly Journal of Applied Mathematics*, 164-168 (1944).

54 Marquardt, D. An Algorithm for Least-Squares Estimation of Nonlinear Parameters. *Journal of the Society for Industrial and Applied Mathematics* **11**, 431-441 (1963).

55 Fedorova, A. *et al.* Solar infrared occultation observations by SPICAM experiment on Mars-Express: Simultaneous measurements of the vertical distributions of H_2O, CO_2 and aerosol. *Icarus* **200**, 96-117 (2009).

56 Warren, S. G. & Brandt, R. E. Optical constants of ice from the ultraviolet to the microwave: A revised compilation. *J. Geophys . Res .* **113**, D14220, doi:doi:10.1029/2007JD009744 (2008).

57 Wolff, M. J. *et al.* Wavelength dependence of dust aerosol single scattering albedo as observed by CRISM. *J. Geophys. Res.* **114**, E00D04, doi:10.1029/2009JE003350 (2009).

58 Fedorova, A. *et al.* Evidence for a bimodal size distribution for the suspended aerosol particles on Mars. *Icarus* **231**, 239-260, doi:http://dx.doi.org/10.1016/j.icarus.2013.12.015 (2014).

59 Hansen, J. E. & Travis, L. D. Light Scattering in Planetary Atmospheres. *Space Sci. Rev.* **16**, 527-610 (1974).

Data availability

The datasets generated by the NOMAD and ACS instruments and analysed during the current study will be available in the ESA PSA repository, https://archives.esac.esa.int/psa, after the proprietary period. The datasets directly used in this study, and especially the data used for the figures, are available from the corresponding author upon reasonable request.

Code availability

The codes used to calculate the dust/aerosols optical depths shown in figure 1 are available upon request to the corresponding author. The code used to inverse the NOMAD and ACS spectra and derive density profiles, have been favourably compared to the Planetary Spectrum Generator (PSG) tool which can be accessed at https://psg.gsfc.nasa.gov/ and which is part of this study. A version of the retrieval code is available at https://psg.gsfc.nasa.gov/helpatm.php#retrieval

Team member list

NOMAD Science Team

Vandaele, Ann Carine , Royal Belgian Institute for Space Aeronomy (IASB-BIRA), Brussels, Belgium
Lopez Moreno, Jose Juan , Instituto de Astrofisica de Andalucia (IAA/CSIC), Granada, Spain
Bellucci, Giancarlo , Istituto di Astrofisica e Planetologia Spaziali (IAPS/INAF), Rome, Italy
Patel, Manish , The Open University, Milton Keynes, United Kingdom
Alonso-Rodrigo, Gustavo, IDR-UPM, Madrid, Spain
Aoki, Shohei, Royal Belgian Institute for Space Aeronomy (IASB-BIRA),, Brussels, Belgium
Altieri, Francesca, Istituto di Astrofisica e Planetologia Spaziali (IAPS/INAF), Rome, Italy
Bauduin, Sophie, University of Brussels, Brussels, Belgium
Bolsee, David, Royal Belgian Institute for Space Aeronomy (IASB-BIRA), Brussels, Belgium
Carrozzo, Giacomo, Istituto di Astrofisica e Planetologia Spaziali (IAPS/INAF), Rome, Italy
Clancy, Todd, Space Science Institute, Boulder, Colorado, USA
Cloutis, Edward, University of Winnipeg, Winnipeg, Manitoba, Canada
Crismani, Matteo, NASA Goddard Space Flight Center (GSFC), Greenbelt, MD, USA
Daerden, Frank, Royal Belgian Institute for Space Aeronomy (IASB-BIRA), Brussels, Belgium
Da Pieve, Fabiana, Royal Belgian Institute for Space Aeronomy (IASB-BIRA), Brussels, Belgium
D'Aversa, Emiliano, Istituto di Astrofisica e Planetologia Spaziali (IAPS/INAF), Rome, Italy
Depiesse, Cedric , Royal Belgian Institute for Space Aeronomy (IASB-BIRA), Brussels, Belgium
Erwin, Justin, Royal Belgian Institute for Space Aeronomy (IASB-BIRA), Brussels, Belgium
Fedorova, Anna, Space Research Institute (IKI), Moscow, Russian Federation
Funke, Bernd, Instituto de Astrofisica de Andalucia (IAA/CSIC), Granada, Spain
Fussen, Didier, Royal Belgian Institute for Space Aeronomy (IASB-BIRA), Brussels, Belgium
Garcia-Comas, Maia, Instituto de Astrofisica de Andalucia (IAA/CSIC), Granada, Spain
Geminale, Anna, Istituto di Astrofisica e Planetologia Spaziali (IAPS/INAF), Rome, Italy
Gérard, Jean-Claude, University of Liège, Brussels, Belgium
Gkouvelis, Leo, University of Liège, Liège, Belgium
Giuranna, Marco, Istituto di Astrofisica e Planetologia Spaziali (IAPS/INAF), Rome, Italy
Gonzalez-Galindo, Francisco, Instituto de Astrofisica de Andalucia (IAA/CSIC), Granada, Spain
Holmes, James, The Open University, Milton Keynes, United Kingdom
Hubert, Benoît, University of Liège, Liège, Belgium
Ignatiev, Nicolai, Space Research Institute (IKI), Moscow, Russian Federation
Kaminski, Jacek, Institute of Geophysics, Polish Academy of Sciences, Warsaw, Poland
Karatekin, Ozgur, Royal Observatory of Brussels, Brussels, Belgium
Kasaba, Yasumasa, Tohoku University, Tohoku, Japan
Kass, David, Jet Propulsion Laboratory, Pasadena, California, USA
Kleinbohl, Armin, Jet Propulsion Laboratory, Pasadena, California, USA
Lanciano, Orietta, ASI, Rome, Italy
Lefèvre, Franck, LATMOS, Paris, France
Lewis, Stephen, The Open University, Milton Keynes, United Kingdom
Liuzzi, Giuliano , NASA Goddard Space Flight Center (GSFC), Greenbelt, MD, USA
López-Puertas, Manuel, Instituto de Astrofisica de Andalucia (IAA/CSIC), Granada, Spain
López-Valverde, Miguel, Instituto de Astrofisica de Andalucia (IAA/CSIC), Granada, Spain
Mahieux, Arnaud , Royal Belgian Institute for Space Aeronomy (IASB-BIRA), Brussels, Belgium
Mason, Jon, The Open University, Milton Keynes, United Kingdom
Mumma, Mike, NASA Goddard Space Flight Center (GSFC), Greenbelt, MD, USA
Nakagawa, Hiromu, Tohoku University, Tohoku, Japan
Neary, Lori, Royal Belgian Institute for Space Aeronomy (IASB-BIRA), Brussels, Belgium
Neefs, Eddy, Royal Belgian Institute for Space Aeronomy (IASB-BIRA), Brussels, Belgium
Novak, R., NASA Goddard Space Flight Center (GSFC), Greenbelt, MD, USA
Oliva, Fabrizio, Istituto di Astrofisica e Planetologia Spaziali (IAPS/INAF), Rome, Italy

Piccialli, Arianna, Royal Belgian Institute for Space Aeronomy (IASB-BIRA), Brussels, Belgium
Renotte, Etienne, ATMOS, Liège, Belgium
Ritter, Birgit, University of Liège, Liège, Belgium
Robert, Séverine, Royal Belgian Institute for Space Aeronomy (IASB-BIRA), Brussels, Belgium
Sindoni, Giuseppe, Istituto di Astrofisica e Planetologia Spaziali (IAPS/INAF), Rome, Italy
Smith, Mike, NASA Goddard Space Flight Center (GSFC), Greenbelt, MD, USA
Thiemann, Ed, LASP, , Boulder, Colorado, USA
Thomas, Ian, Royal Belgian Institute for Space Aeronomy (IASB-BIRA), Brussels, Belgium
Trokhimovskiy, Sacha, Space Research Institute (IKI), Moscow, Russian Federation
Trompet, Loïc, Royal Belgian Institute for Space Aeronomy (IASB-BIRA), Brussels, Belgium
Vander Auwera, Jean, University of Brussels, Brussels, Belgium
Villanueva, Geronimo, NASA Goddard Space Flight Center (GSFC), Greenbelt, MD, USA
Viscardy, Sébastien, Royal Belgian Institute for Space Aeronomy (IASB-BIRA), Brussels, Belgium
Whiteway, Jim, York University, Toronto, Ontario, Canada
Wilquet, Valerie , Royal Belgian Institute for Space Aeronomy (IASB-BIRA), Brussels, Belgium
Willame, Yannick, Royal Belgian Institute for Space Aeronomy (IASB-BIRA), Brussels, Belgium
Wolff, Michael, Space Science Institute, Boulder, Colorado, USA
Wolkenberg, Paulina, Istituto di Astrofisica e Planetologia Spaziali (IAPS/INAF), Rome, Italy
Yelle, Roger, LPL, Tucson, Arizona, USA

ACS Science Team
Altieri, Francesca, Istituto di Astrofisica e Planetologia Spaziali (IAPS/INAF), Rome, Italy
Arnold, Gabriele, Institute of Planetary Research, DLR, Berlin, Germany
Baggio, Lucio, LATMOS, Paris, France
Belyaev, Denis, Space Research Institute (IKI), Moscow, Russian Federation
Bertaux, Jean-Loup, LATMOS, Paris, France
Duxbury, Natalia, Russian Federation, Moscow University
Fedorova, Anna, Space Research Institute (IKI), Moscow, Russian Federation
Forget, François, LMD, Paris, France
Fouchet, Thierry, LESIA, OBSPM , Paris, France
Grassi, Davide, Istituto di Astrofisica e Planetologia Spaziali (IAPS/INAF), Rome, Italy
Grigoriev, Alexey Space Research Institute (IKI), Moscow, Russian Federation
Guerlet, Sandrine, LMD, Paris, France
Hartogh, Paul, Germany, Max-Planck-Institut für Sonnensystemforschung
Ignatiev, Nikolay, Space Research Institute (IKI), Moscow, Russian Federation
Kasaba, Yasumasa, Japan, Dep. Geophysics, Graduate School of Science, Tohoku University
Khatuntsev , Igor, Space Research Institute (IKI), Moscow, Russian Federation
Korablev, Oleg, Space Research Institute (IKI), Moscow, Russian Federation
Krasnopolsky, Vladimir, Russian Federation, MIPT
Kuzmin, Ruslan, Russian Federation, Vernadsky Institute
Lefèvre, Franck, LATMOS, Paris, France
Lellouch, Emmanuel, LESIA, OBSPM , Paris, France
Lopez-Valverde, Miguel, Instituto de Astrofisica de Andalucia (IAA/CSIC), Granada, Spain
Määttänen, Anni, LATMOS, Paris, France
Marcq, Emmanuel, LATMOS, Paris, France
Martin-Torres, Javier, Lulea University, Lulea, Sweden
Medvedev, Alexander, Max-Planck-Institut für Sonnensystemforschung, Göttingen, Germany
Montmessin, Franck, LATMOS, Paris, France
Moshkin, Boris, Space Research Institute (IKI), Moscow, Russian Federation
Patel, Manish, The Open University, Milton Keynes, United Kingdom
Rodionov, Daniel, Space Research Institute (IKI), Moscow, Russian Federation

Rodin, Alexander, Moscow Institute of Physics and Technology, Moscow (*MIPT*), Moscow, Russian Federation
Shakun, Alexey, Space Research Institute (IKI), Moscow, Russian Federation
Shematovich, Valery, Institute of Astronomy, RAS, Moscow, Russian Federation
Thomas, Ian, Royal Belgian Institute for Space Aeronomy (IASB-BIRA), Brussels, Belgium
Thomas, Nicolas, Physikalisches Institut, University of Bern, Bern, Switzerland
Trokhimovsky, Alexander, Space Research Institute (IKI), Moscow, Russian Federation
Vazquez, Luis, UMC, Madrid, Spain
Vincendon, Matthieu, IAS, Université Paris Sud, Paris, France
Wilquet, Valérie, Royal Belgian Institute for Space Aeronomy (IASB-BIRA), Brussels, Belgium
Wilson, Colin, Oxford University, Oxford, United Kingdom
Zasova, Ludmila, Space Research Institute (IKI), Moscow, Russian Federation
Zelenyi, Lev, Space Research Institute (IKI), Moscow, Russian Federation
Zorzano, Maria Paz, Lulea University, Lulea, Sweden
Anufreychik, Konstantin, Space Research Institute (IKI), Moscow, Russian Federation
Kokonkov, NIkita, Space Research Institute (IKI), Moscow, Russian Federation
Lacombe, Gaétan, LATMOS, Paris, France
Maslov, Igor, Space Research Institute (IKI), Moscow, Russian Federation
Patrakeev, Andrey, Space Research Institute (IKI), Moscow, Russian Federation
Patsaev, Dimitry, Space Research Institute (IKI), Moscow, Russian Federation
Alday , Juan, Oxford University, Oxford, United Kingdom
Luginin, Mikhael Space Research Institute (IKI), Moscow, Russian Federation
Olsen, Kevin, LATMOS, Paris, France

Extended Data - Figure captions

ED Figure 1: Continuum optical depth vs latitude and solar longitude. The colour denotes the lowest altitude at which the optical depth is less than 1.0, i.e. the lowest altitude where sunlight can still penetrate the atmosphere easily. There is a strong latitudinal dependence, where northern and southern high latitudes are relatively clear until the line of sight drops below 10-15km (blue and dark blue) – except during the Ls = 200° – 240° period where the global dust storm appears to have raised this altitude to 20-25km (light blue and cyan).

ED Figure 2: Impact of the dust storm on NOMAD LNO nadir observations. The calibrated radiance at 2.3 μm is shown for two orbits before (Panel a) and during (Panel b) the dust event as a function of the latitude. In red, the comparison to a radiative transfer model is also presented. The dust opacity before the global dust storm is τ=0.46 at 3 μm, while during the event, there is an increase by at least of a factor 10 (τ=4.6). The 1-sigma error of the data is 8.2×10^{-5} W/m2/sr/cm^{-1}. Panel c shows the surface albedo, in black OMEGA albedo at 2.33 μm (order 190), in red TES bond albedo scaled to the OMEGA one.

ED Figure 3: Atmospheric transmittances measured by NOMAD during the storm (Ls = 196.64° – Lat = 51° – Lon = 148°E) showing HDO absorption features (arrows) appearing at tangent heights up to 50 km; most of the other absorption features originate from CO_2.

ED Figure 4: Example of results of the H_2O retrieval from NOMAD. Top panel: black: transmittance measured at the tangent height of 22.2 km; blue: best fit; cyan and green: different simulations with 1 ppm and 100 ppm water respectively. Bottom panel: residuals between the observation and the best fit. The error for transmittance were calculated from 1-sigma noise value.

ED Figure 5: Example of results of the H_2O retrieval from ACS NIR. Top panel: black: transmittance measured at the tangent height of 34.1 km; blue: best fit; cyan, red, and green: different simulations with no water, 1 ppm and 50 ppm water respectively. Bottom panel: residuals between the observation and the best fit. The error for transmittance were calculated from 1-sigma noise value.

ED Figure 6: Extinction of water ice with different particle sizes (Panel A) and slant optical depth (Panel B, in units of km^{-1}) for the solar occultation performed by NOMAD before the dust storm, on 7 May between 05.40 and 05.46 UTC (local time 18h), which covers the latitude range 44° N to 57° N and the longitude range -122.6° E to -121.4° E.

ED Figure 7: Illustration of the independent retrieval of dust and water ice from the TIRVIM dataset for a typical southern hemisphere occultation (20.06.2018; Lat 81°N; Lon -66°E; egress): a selection of transmission profiles at 5 wavelengths (left), corresponding to slant opacities (top left) and extinction profiles (top right), retrieved effective radius (r_{eff} in µm, bottom right) and aerosol number density (in cm^{-3}, bottom right). The occultation has been performed on June 20th at orbit 2556 (local time 21:25), and covers the latitude range 81°N to 82°N and the longitude range -67°E to -60°E. The observation corresponds to the MIR H_2O-HDO profiles during the dust storm (yellow curves of Fig.3). The water ice and dust are well distinguished using the 3 µm water ice absorption band (wavenumber 3263 cm^{-1} in the figure). In this case the water ice cloud is detected at 25-30 km. All reported errors are 1-sigma.

Table caption

ED Table 1: Overview of the NOMAD and ACS observations of H_2O and HDO used and shown in this study.

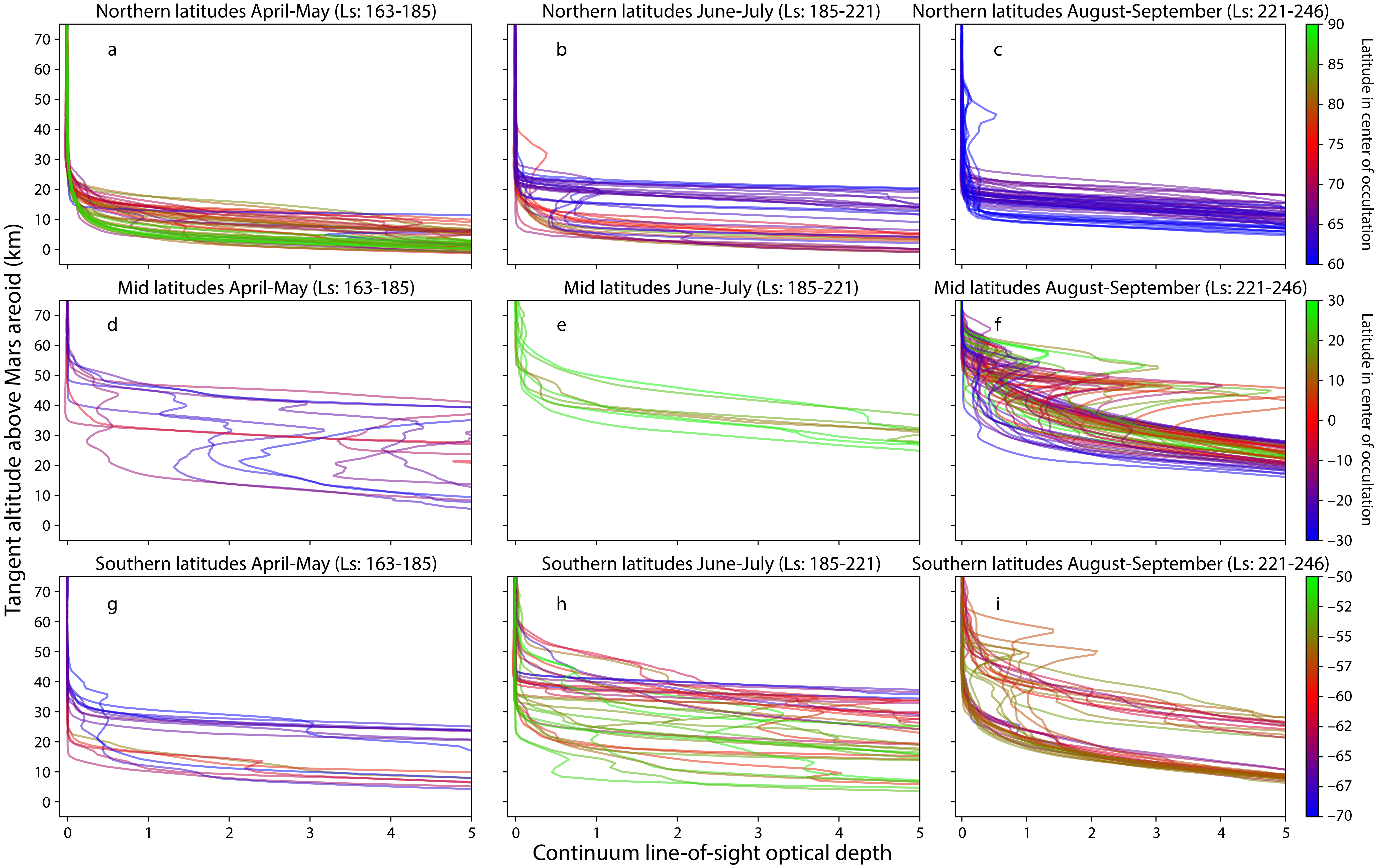
Continuum line-of-sight optical depths for SO diffraction order 121:
Variations by time and tangent point latitude

Northern latitudes April-May (Ls: 163-185)

Northern latitudes June-July (Ls: 185-221)

Northern latitudes August-September (Ls: 221-246)

Mid latitudes April-May (Ls: 163-185)

Mid latitudes June-July (Ls: 185-221)

Mid latitudes August-September (Ls: 221-246)

Southern latitudes April-May (Ls: 163-185)

Southern latitudes June-July (Ls: 185-221)

Southern latitudes August-September (Ls: 221-246)

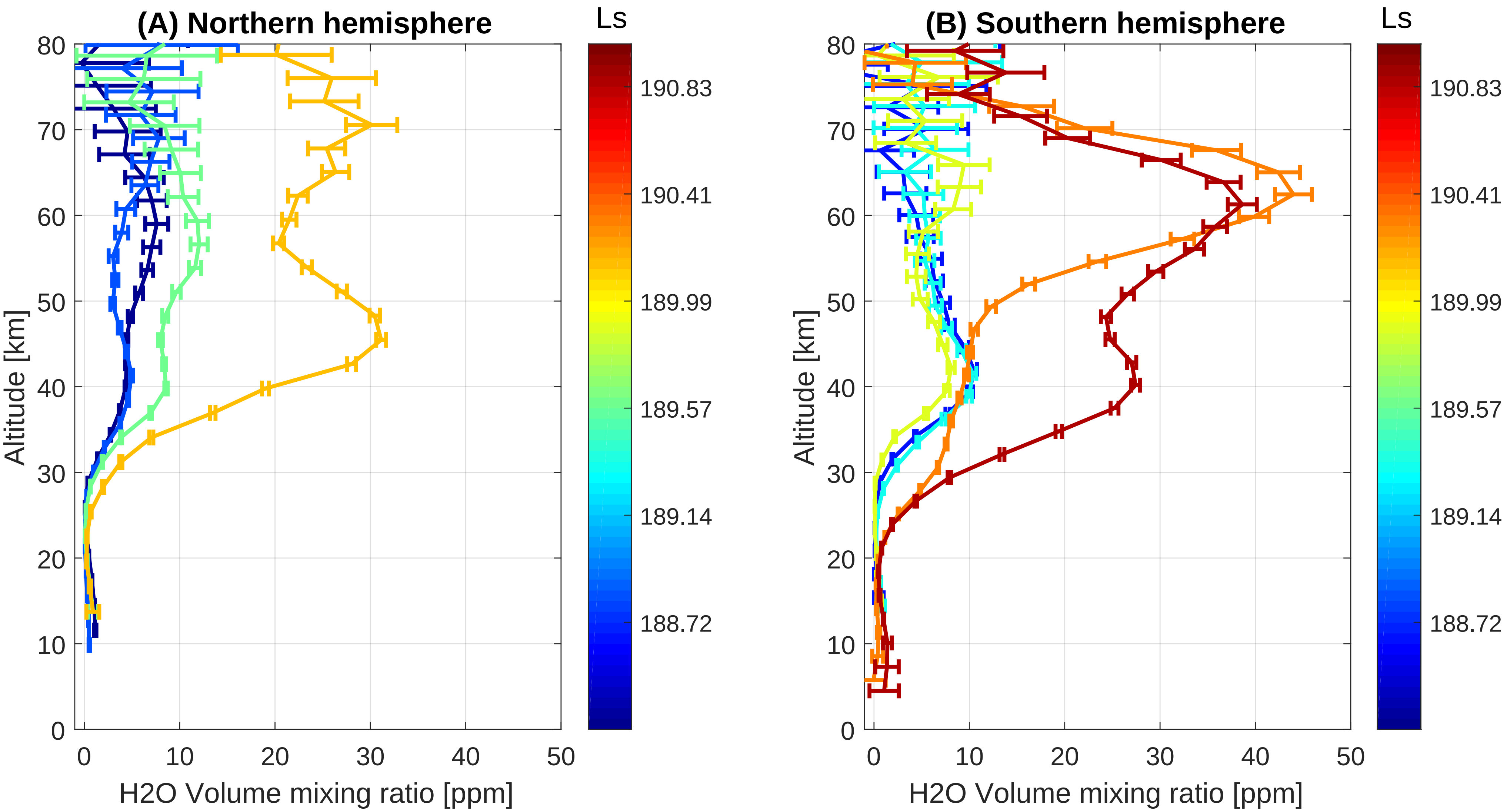
(A) Northern hemisphere
(B) Southern hemisphere
Ls
190.83
190.41
189.99
189.57
189.14
188.72
Altitude [km]
0
10
20
30
40
50
60
70
80
H2O Volume mixing ratio [ppm]
0
10
20
30
40
50

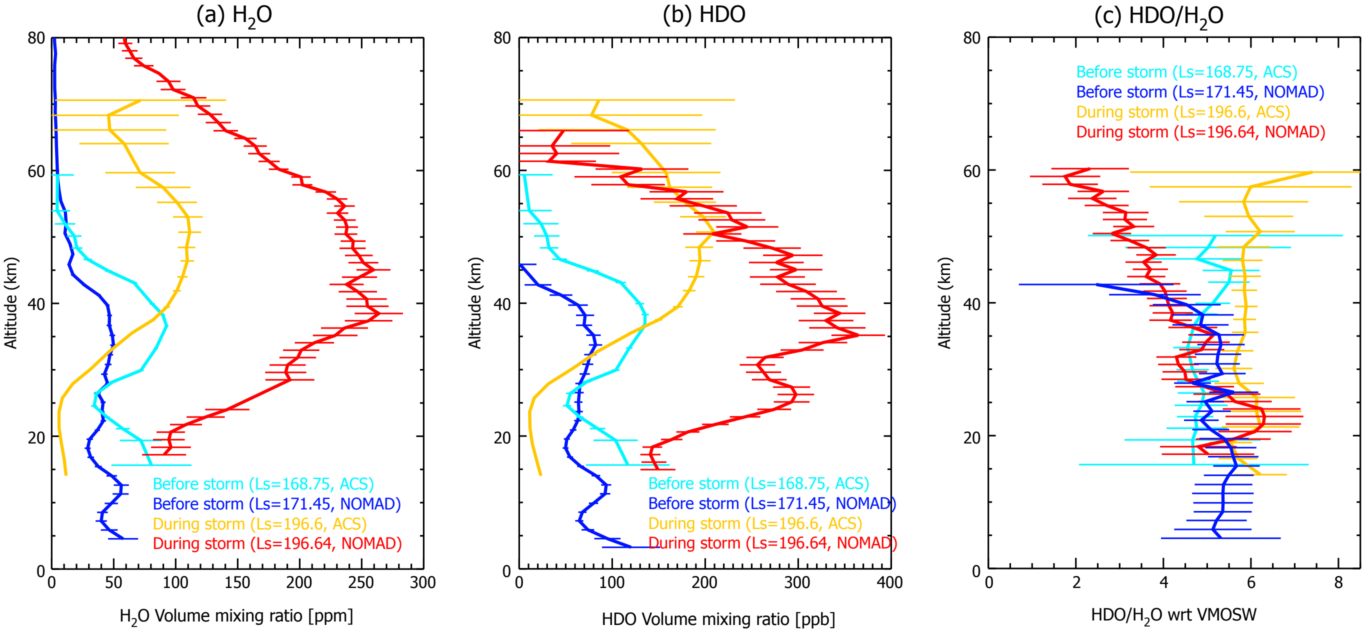
(a) H_2O
(b) HDO
(c) HDO/H_2O
Altitude (km)
H_2O Volume mixing ratio [ppm]
HDO Volume mixing ratio [ppb]
HDO/H_2O wrt VMOSW
0
20
40
60
80
0
50
100
150
200
250
300
0
100
200
300
400
0
2
4
6
8
Before storm (Ls=168.75, ACS)
Before storm (Ls=171.45, NOMAD)
During storm (Ls=196.6, ACS)
During storm (Ls=196.64, NOMAD)